Temperature effects in the hyperfine spectrum of the $D1$ transition of sodium

R. S. Gurjar and K. K. Sharma
Department of Physics and Center for Laser Technology, Indian Institute of Technology, Kanpur 208016, India
(Received 6 April 1998)

The velocity selective optical pumping technique has been used to obtain the Doppler-free spectrum of the $D1$ transition of sodium in the temperature range 110–169 °C. The pump-induced changes in probe transmission across the Lamb dip and crossover resonances first increase and then decrease with temperature. We also observe a reversal in the relative magnitudes of these changes among some of the narrow resonances. These and other temperature-dependent features of the Doppler-free spectrum of the $D1$ transition of sodium are successfully explained within the framework of the composite five-level model. The degeneracies of the ground-state composite levels and the beam depletion effects at higher temperatures play a crucial role in these investigations. [S1050-2947(98)05011-2]

PACS number(s): 33.80.Be, 32.30.−r, 32.70.Jz

I. INTRODUCTION

The high-resolution spectroscopy of the $D1$ transition of sodium obtained in a low-vapor pressure cell has recently been analyzed in terms of an effective five-level model [1]. The technique of the velocity selective optical pumping (VSOP) was used in this study to eliminate first-order Doppler broadening. The success of this technique to reveal natural or subnatural line profiles of atomic transitions critically depends on the enhanced absorption of the probe beam in the wings of a Doppler-broadened profile as compared to the absorption at the center of the profile in the presence of a relatively strong counterpropagating pump beam. As shown by Svanberg *et al.* [2], large absorption lengths are needed to record high contrast probe transmission in a VSOP experiment. The required absorption lengths can be achieved by using long vapor cells (cells as long as 30 cm have been used) or by the use of cells of moderate lengths but at somewhat higher vapor pressures. The later choice, however, runs the risk of increased pressure broadening. On the other hand, uniform beam profiles may be difficult to maintain across long cells. The high-vapor pressure (or equivalently high temperature) cells, however, require the use of relatively stronger pump beams to overcome increased beam depletion. Although somewhat sharper line profiles at 169 °C cell temperature were reported in the 10-cm-long cell used by the authors of Ref. [1], the detailed analysis of the results was restricted to their low-temperature measurements in the neighborhood of 120 °C. There is a growing interest at the present moment in recording and understanding subnatural linewidths [3–5]. In a related context, Lukin *et al.* [6] have reported subnatural line features in an electromagnetically induced transparency (EIT) window. To investigate natural or subnatural line profiles of atomic transitions, it is necessary to work at higher temperatures for cells of moderate lengths. Here, we report some unusual features in the Doppler-free spectrum of the sodium $D1$ transition found in the temperature range of 110 to 169 °C. The new approach, presented here for the interpretation of results, has removed some of the inadequacies of the previous investigation and we find considerably improved agreement between the theoretical and experimental results at low, intermediate, and relatively high cell temperatures. In Sec. II, we review the composite five-level model in the context of the sodium $D1$ transition. Section III deals with experimental details. Beam propagation in a dense medium is discussed in Sec. IV. Spectral changes with temperature are presented in Sec. V, followed by a discussion of linewidths and the sum rules. The paper ends with a brief summary of our findings.

II. SODIUM $D1$ TRANSITION

The hyperfine (hf) structure of the $D1$ transition of sodium is shown in Fig. 1. The ground state $^2S_{1/2}$ splits into two hyperfine levels with $F_g=1,2$ separated by 1772 MHz. The corresponding splitting of the excited state $^2P_{1/2}$ is 189 MHz. The magnetic sublevels associated with each hf level are $(2F+1)$-fold degenerate in the absence of an external

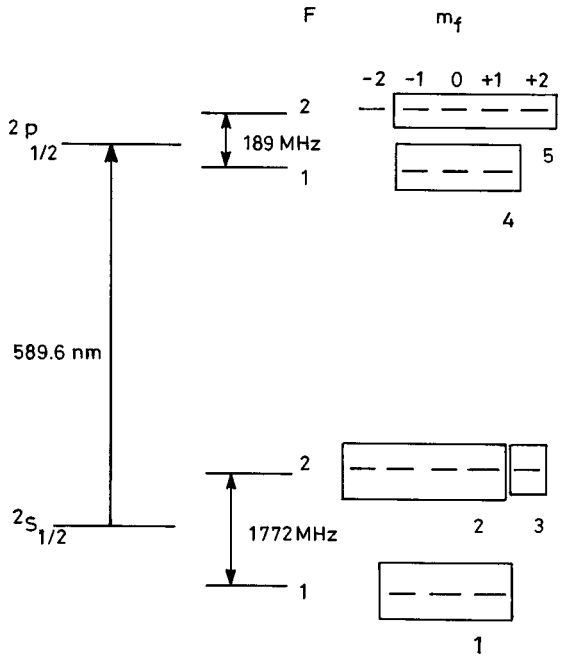

FIG. 1. Hyperfine spectrum of $D1$ transition of sodium. The grouping of the magnetic sublevels for the five composite level model is indicated.

TABLE I. Transitions ($i \rightarrow j$) contributing to the narrow resonances. LD1 to LD4 are the Lamb-dip resonances and CR5 to CR9 are the crossover resonances.

	LD1	LD2	LD3	LD4	CR5	CR6	CR7	CR8	CR9
$i \rightarrow j$	2-4	2-5	1-4	1-5	2-4	2-4	2-4	2-5	1-4
					2-5	1-4	2-5	1-5	1-5
							1-5		
							2-5		

magnetic field. A right circularly polarized (σ^+) beam will induce transitions with the selection rule $\Delta m_f = +1$. All ground-state magnetic sublevels except the one with $F=2$, $m_f=2$ will absorb this radiation. As a consequence, substantial atomic population builds up in this level as a result of optical pumping. The five composite levels [7] needed for interpreting the experimental results are labeled 1 to 5 in Fig. 1. Since no transition with this choice of the polarization state connects any of the ground levels to the $F=2$, $m_f=-2$ sublevel of the excited state, this level is ignored altogether in the subsequent discussion. For a given velocity group, the steady-state populations of the relevant composite levels in the presence of a right circularly polarized pump beam have been obtained by solving a set of rate equations in [1] and are reproduced below,

$$N_1 = N_1^0 + S_{14}^1 \mathcal{L}'_{14} + S_{15}^1 \mathcal{L}'_{15} + S_{24}^1 \mathcal{L}'_{24} + S_{25}^1 \mathcal{L}'_{25}, \quad (1)$$

$$N_2 = N_2^0 + S_{14}^2 \mathcal{L}'_{14} + S_{15}^2 \mathcal{L}'_{15} + S_{24}^2 \mathcal{L}'_{24} + S_{25}^2 \mathcal{L}'_{25}, \quad (2)$$

$$N_4 = S_{14}^4 \mathcal{L}'_{14} + S_{24}^4 \mathcal{L}'_{24}, \quad (3)$$

$$N_5 = S_{15}^5 \mathcal{L}'_{15} + S_{25}^5 \mathcal{L}'_{25}, \quad (4)$$

where

$$\mathcal{L}'_{ij} = \frac{(\gamma_H/2)^2}{(\Delta_{ij} - x)^2 + (1 + S_{ij})(\gamma_H/2)^2} \quad (5)$$

and N_i and N_i^0 appearing in the above equations represent velocity-dependent population densities $N_i(x)$ and $N_i^0(x)$ of the ith level in the presence and absence of the pump beam, respectively. Here, $N_i^0(x) = N_{i,0} G(x)$, where $N_{i,0}$ is the total number of atoms at thermal equilibrium in the ith level and $G(x)$ represents the normalized Gaussian distribution function $(1/\sqrt{\pi} ku) e^{-(x/ku)^2}$, where u is the most probable velocity and k is the Boltzmann constant; $\gamma_H = 1/\tau + 2/T$ represents the homogeneous linewidth of the i-j transition, where τ is the lifetime of the transition in question, T (not to be confused with temperature) appearing here and in subsequent equations refers to the time for the population of the pumped level 3 to thermalize, Δ_{ij} represents the laser detuning with respect to the transition frequency ω_{ij}; $x = 2\pi v/\lambda$, where v is the axial atomic velocity and S_{ij} and S_{ij}^k are defined in the Appendix. We have not included level 3 in the above equations because, although this level plays a crucial role in the redistribution of atomic populations, no absorption of the right circularly polarized beam is possible from this level. As described in Ref. [1], the VSOP measurement yields in all nine narrow resonances including four Lamb-dip resonances (1-4, 1-5, 2-4, and 2-5) and five crossover resonances. The former group of resonances arises when the pump and the probe beams simultaneously interact with axially stationary atoms. The latter resonances exist for special velocity groups for which the upshifted pump and the downshifted probe or *vice versa* are simultaneously in resonance with any two distinct transitions from among the four possible transitions within the $D1$ manifold. For example, it may happen that the upshifted pump may connect the 1-5 transition and the downshifted probe is in resonance with the 2-4 transition. The Lamb-dip resonances have been designated as LD1 to LD4 and the crossover resonances as CR5 to CR9 in order of increasing frequency. The specific transitions involved in these resonances are shown in Table I.

III. EXPERIMENTAL DETAILS

Circularly polarized pump and probe beams having the same sense (σ^+) of polarization were made to counterpropagate in a 10-cm-long sodium cell and the probe beam transmission was recorded as a function of laser detuning at various temperatures. The cell temperature was not controlled precisely but it was monitored to be stable to within 2 °C. The sodium cell did not contain any buffer gas. Our measurements were restricted to the temperature interval 110–169 °C. The counterpropagating pump and the probe beams were derived from the same single-mode tunable Ring Dye laser Coherent Model 699-21. The split beams were expanded by a long focal length lens so that the pump and the probe beam diameters over the length of the cell were nearly 5 and 2 mm, respectively. The beams were polarized using λ/4 plates. The input pump and the probe beam powers throughout these experiments were kept at 200 and 1 μW, respectively. These values correspond to pump and probe intensities at the entrance of the cell to about 10.0 and 0.3 μW/mm^2, respectively. The probe transmission measurements were carried out under well established steady-state conditions. Lock-in detection was used to improve the sensitivity of our measurements. Further, the lock-in detection permits us to record only the changes (increase or decrease) in the absorption of the selected velocity groups representing the Lamb dips and the crossover resonances arising due to the presence of the pump beam. To get a feel for the kind and extent of spectral changes involved, we have reproduced some of the recorded resonances in Fig. 2. From this figure it is seen that at the lower temperature (110 °C), the first set of narrow resonances, namely LD1, CR5, and LD2, are somewhat stronger than the corresponding resonances in the set consisting of the LD3, CR9, and LD4 resonances. The lock-in detection sensitivities used for recording different groups of resonances were different, but Fig. 2 has been

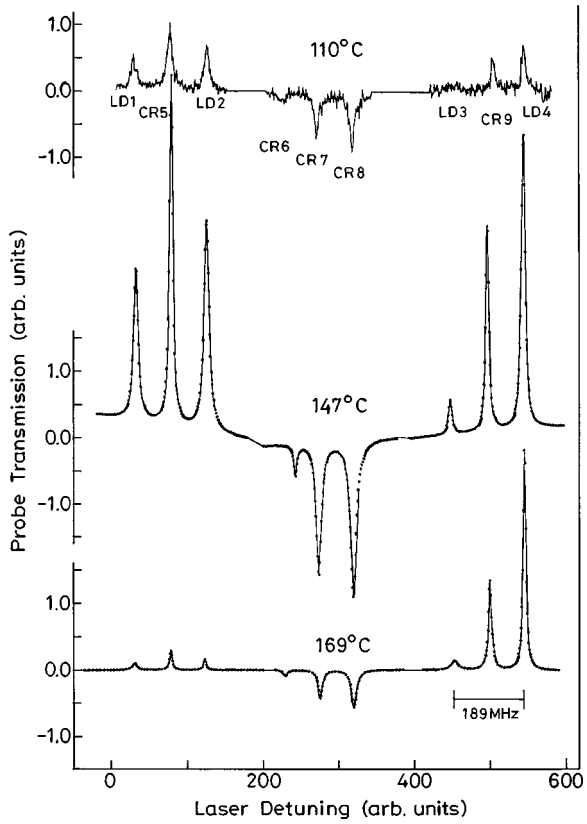

FIG. 2. Normalized profiles of the Doppler-free spectrum of the $D1$ transition of sodium observed at 110, 147, and 169 °C. The Lamb-dip resonances are marked LD1 to LD4 and the crossover resonances as CR5 to CR9.

normalized so that the peak heights correctly reflect the relative strengths of the resonances. At the higher temperature, say 169 °C, a reversal of this behavior occurs, i.e., the LD3, CR9, and LD4 resonances which were earlier somewhat weaker than the LD1, CR5, and LD2 resonances at 110 °C have now grown in strength while the resonances in the first set are quite weak at this higher temperature. Such behavior seems strange at first sight considering the fact that the density effects should play similar roles for the populations of the two ground hyperfine levels. The thermal energy kT even at room temperature is much larger than the ground-state hyperfine (hf) splitting. One might think that the populations of the hf levels 1 and 2 should equalize, leading to no relative changes in the intensities of the transitions starting from the two ground levels as the temperature is changed. This would actually be the case if levels 1 and 2 had equal degeneracies. However, the relative populations of the composite levels 1 and 2 can differ significantly because they have different degeneracies. It is not obvious at this stage how any difference in the degeneracy of the two ground levels can lead to the reversal of the relative strengths of the two groups of resonances. Further, there is another peculiar aspect of the thermal behavior of these resonances which can be noticed from Fig. 2. We find that the probe transmission is noticeably higher at the intermediate temperature of 147 °C as compared to the probe transmissions at the extreme temperatures. This nonmonotonic behavior of the probe transmission as a function of temperature (or the number density) appears equally intriguing at first sight.

IV. BEAM PROPAGATION IN DENSE VAPOR

A linear relationship between the changes in the absorption coefficient of the cell and changes in the transmittance of a weak probe due to the presence of a relatively strong pump can be obtained from the linearized Beer-Lambert law,

$$\frac{I_t(p)-I_t(0)}{I_0}=\alpha(0)L-\alpha(p)L. \tag{6}$$

Here, $I_t(0)/I_0$ and $\alpha(0)$ are, respectively, the probe transmittance and the probe absorption coefficient in the absence of the pump beam, $I_t(p)/I_0$ and $\alpha(p)$ are the corresponding quantities in the presence of the pump, and L is the cell length. In the absence of the pump, the probe beam absorbance was found to be 11% at 110 °C and 96% at 169 °C, indicating substantial beam depletion at both temperatures. The $\alpha_0 L$ values at these temperatures are 0.11 and 3.2, respectively. We shall formulate this problem in two stages. First, we consider the propagation of the pump beam alone and then bring in the counterpropagating probe beam to monitor the pump-induced changes in the absorption coefficient. This method takes into account exactly the effects of the pump depletion as it propagates in the cell. In view of substantial beam absorption in our 10-cm-long cell even at temperatures as low as 110 °C, linearization of the Beer-Lambert law across the entire cell length is not valid. Further and more importantly, the atoms further down from the beam entrance end of the cell see weaker and weaker pump beam. As a consequence, the extent of optical pumping decreases from the entrance-end to the exit-end of the cell. This will lead to nonuniform absorption of the probe beam as it traverses the cell from the opposite direction. In fact, at higher temperatures the probe beam may get heavily attenuated in the initial stages for lack of significant optical pumping in that region. Our calculations must take account of these effects. It is necessary, therefore, to divide the cell into a sufficiently large number of subcells so that the beam depletion across each cell is rather small. We then apply the Beer-Lambert law across each subcell. The beam transmitted by one subcell becomes the incident beam for the next subcell and so on. In this manner the beam depletion effects are fully incorporated. Similar considerations were applied by Caiyan *et al.* [8] to the Doppler-free spectrum of the $D1$ transition in sodium, though their aim was to study the effect of beam propagation on the linewidths of the resonances. As the pump beam enters the cell, it begins to disturb the Boltzmann distribution of atomic levels. Eventually a new steady-state population distribution is achieved. For the present study, we ignore the transient stage of population buildup and deal with only the steady-state populations of levels. We now calculate how the pump beam gets attenuated as it traverses the cell after the steady state has been attained.

A. Pump absorption coefficient

We begin by dividing the cell length into N equal slices. Our aim is to first calculate the actual pump intensity that each group of atoms sees inside each slice and then calculate the extent of optical pumping produced throughout the length of the cell. Subsequently in a similar manner we shall consider the propagation of the probe beam which monitors

the extent of optical pumping in each slice. Applying the differential form of the Beer-Lambert law to the nth slice, we have

$$\frac{dI_n}{dz} = -\alpha_n I_n, \tag{7}$$

where α_n is the absorption coefficient of the nth slice as seen by the pump. For sufficiently small thickness Δz of each slice, Eq. (7) can be integrated to give

$$I_{n+1}(\text{in}) = I_n(\text{out}) = I_n(\text{in}) e^{-\alpha_n(I_n)\Delta z}. \tag{8}$$

We can now write for the absorption coefficient of the nth slice,

$$\begin{aligned}\alpha_n^{\text{pump}}(\nu) = \alpha_n(I) = &\int (N_1 - N_4)\overline{\sigma}_{14}\mathcal{L}_{14}dx \\ &+ \int (N_1 - N_5)\overline{\sigma}_{15}\mathcal{L}_{15}dx \\ &+ \int (N_2 - N_4)\overline{\sigma}_{24}\mathcal{L}_{24}dx \\ &+ \int (N_2 - N_5)\overline{\sigma}_{25}\mathcal{L}_{25}dx,\end{aligned} \tag{9}$$

where

$$\mathcal{L}_{ij}(x) = \frac{(\gamma_H/2)^2}{(\Delta_{ij} - x)^2 + (\gamma_H/2)^2} \tag{10}$$

and N_i are the velocity-dependent steady-state population densities in the presence of the pump beam within the nth slice and integration is over the atomic velocities through the already defined parameter x. The average cross section $\overline{\sigma}_{ij}$ of a given m_f sublevel belonging to a particular composite level is defined as σ_{ij}/g_i, where g_i is the m_f degeneracy of the lower level of the transition. The cross sections σ_{ij} for the composite levels of sodium appear in Table II. In writing this expression for the absorption coefficient of the cell we have acknowledged the fact that because of Doppler broadening, all transitions among the hyperfine levels contribute to absorption at frequency ν. We have written the superscript ''pump'' in Eq. (9) to remind us that at this stage, we are dealing with the pump beam alone. We have explicitly introduced the frequency dependence of the absorption coefficient because this integral is to be solved for a particular value of the laser frequency. Knowing $\alpha_n(I)$ after solving the relevant integrals in Eq. (9), we can compute I_{n+1} using Eq. (8). For the next slice we use this I_{n+1} to calculate $\alpha_{n+1}(I)$ and use the absorption coefficient so obtained iteratively to calculate the input intensity for the next slice and so on. In this manner we generate values for the input intensities for each slice.

TABLE II. Relevant cross sections and degeneracies for the D_1 transition.

Transition $i \rightarrow j$	g_i	σ_{ij} [units of $\pi\lambda\!\!\!^{-2}(\gamma_N/\gamma_H)$]
1-4	4	1/3
1-5	4	5/3
2-4	3	5/3
2-5	3	5/3

We now proceed to calculate the pump absorption in the nth slice at a frequency lying anywhere within the overall limits of the $D1$ transition. On substituting expressions for N_1 to N_5 from Eqs. (1)–(4) we find that the 20 integrals appearing in Eq. (9) involve either single or double Lorentzians. The integrals involving double Lorentzians fall into two categories. The first kind have the same central frequency whereas the second kind involve double Lorentzians centered at relatively far-off frequencies. The latter kind of integrals will not contribute much to pump absorption as the products of such Lorentzians are essentially zero because of their extremely narrow widths. With these observations, we need to retain only the following eight integrals in the expression for the pump absorption coefficient:

$$\begin{aligned}\alpha^{\text{pump}}(\nu, I_{\text{pump}}) = &-\int_{-\infty}^{\infty} \overline{\sigma}_{14}\left(\frac{T\tau_e\sigma_{14}4N_{1,0}G(x)}{12h\nu T} - S_{14}^1\right)\mathcal{L}'_{14}(x)\mathcal{L}_{14}(x)dx + \int_{-\infty}^{\infty} N_{1,0}G(x)\sigma_{14}\mathcal{L}_{14}(x)dx \\ &-\int_{-\infty}^{\infty} \overline{\sigma}_{15}\left(\frac{T\tau_e\sigma_{15}4N_{1,0}G(x)}{12h\nu T} - S_{15}^1\right)\mathcal{L}'_{15}(x)\mathcal{L}_{15}(x)dx + \int_{-\infty}^{\infty} N_{1,0}G(x)\sigma_{15}\mathcal{L}_{15}(x)dx \\ &-\int_{-\infty}^{\infty} \overline{\sigma}_{24}\left(\frac{T\tau_e\sigma_{24}3N_{2,0}G(x)}{12h\nu T} - S_{24}^2\right)\mathcal{L}'_{24}(x)\mathcal{L}_{24}(x)dx + \int_{-\infty}^{\infty} N_{2,0}G(x)\sigma_{24}\mathcal{L}_{24}(x)dx \\ &-\int_{-\infty}^{\infty} \overline{\sigma}_{25}\left(\frac{T\tau_e\sigma_{25}3N_{2,0}G(x)}{12h\nu T} - S_{25}^2\right)\mathcal{L}'_{25}(x)\mathcal{L}_{25}(x)dx + \int_{-\infty}^{\infty} N_{2,0}G(x)\sigma_{25}\mathcal{L}_{25}(x)dx.\end{aligned} \tag{11}$$

It should also be noted that the Gaussians $G_i(x)$ are also centered at different frequencies but they have much broader spread as compared to the Lorentzians. The four integrals in Eq. (11) involving single Lorentzians represent the thermal equilibrium contribution to the absorption coefficient at a particular frequency as a result of 1-4, 1-5, 2-4, and 2-5 excitations, respectively. If the laser was tuned to, say, the 1-4 transition, then clearly the longitudinally stationary atoms contribute to the absorption coefficients through the 1-4 transition but atoms which are appropriately Doppler shifted contribute through the remaining three transitions. The remaining four integrals in Eq. (11) represent absorption (rather the lack of it and hence the opposite sign) by atoms which have been pumped out (removed) by the 1-4, 1-5, 2-4, and 2-5 optical pumping cycles and transferred to other levels, in particular to level 3 in the five-level scheme. Once again for these terms as well, longitudinally stationary atoms contribute to the 1-4 transition and appropriately Doppler-shifted atoms contribute to the remaining three transitions. The integrals were evaluated as follows. The presence of the narrow Lorentzians (10–15 MHz) in Eq. (11) suggests that the dominant contributions to the integrals come from narrow ranges of velocities over which the Gaussian factors $G(x)$ hardly change. This allows us to take constant values for the Gaussian factors during the process of integration. The complete expression for the pump absorption coefficient (for the nth slice) at this frequency then takes the form

$$\alpha^{\text{pump}}(\nu,I_{\text{pump}}) = -\frac{(\gamma_H/2)\pi(\sqrt{1+S_{14}}-1)}{S_{14}\sqrt{1+S_{14}}}\frac{T(1/\tau+2/T-\Gamma_{41})}{3(1/\tau+1/T)}\frac{\sigma_{14}\bar{\sigma}_{14}(\pi\lambda)^2 I}{h\nu}\left(\frac{\gamma_N}{\gamma_H}\right)^2\frac{1}{ku\sqrt{\pi}}\times\exp-\left(\frac{\omega-\omega_{14}}{ku}\right)^2\times N_1^0$$

$$-\frac{(\gamma_H/2)\pi(\sqrt{1+S_{15}}-1)}{S_{15}\sqrt{1+S_{15}}}\frac{T(1/\tau+2/T-\Gamma_{51})}{3(1/\tau+1/T)}\frac{\sigma_{15}\bar{\sigma}_{15}(\pi\lambda)^2 I}{h\nu}\left(\frac{\gamma_N}{\gamma_H}\right)^2\frac{1}{ku\sqrt{\pi}}\times\exp-\left(\frac{\omega-\omega_{15}}{ku}\right)^2\times N_1^0$$

$$-\frac{(\gamma_H/2)\pi(\sqrt{1+S_{24}}-1)}{S_{24}\sqrt{1+S_{24}}}\frac{T(1/\tau+2/T-\Gamma_{42})}{4(1/\tau+1/T)}\frac{\sigma_{24}\bar{\sigma}_{24}(\pi\lambda)^2 I}{h\nu}\left(\frac{\gamma_N}{\gamma_H}\right)^2\frac{1}{ku\sqrt{\pi}}\times\exp-\left(\frac{\omega-\omega_{24}}{ku}\right)^2\times N_2^0$$

$$-\frac{(\gamma_H/2)\pi(\sqrt{1+S_{25}}-1)}{S_{25}\sqrt{1+S_{25}}}\frac{T(1/\tau+2/T-\Gamma_{52})}{4(1/\tau+1/T)}\frac{\sigma_{25}\bar{\sigma}_{25}(\pi\lambda)^2 I}{h\nu}\left(\frac{\gamma_N}{\gamma_H}\right)^2\frac{1}{ku\sqrt{\pi}}\times\exp-\left(\frac{\omega-\omega_{25}}{ku}\right)^2\times N_2^{(0)}$$

$$+\left[\left(\tfrac{5}{8}\right)N_{\text{total}}^{(0)}(\bar{\sigma}_{14}+\bar{\sigma}_{15})+\left(\tfrac{3}{8}\right)N_{\text{total}}^{(0)}(\bar{\sigma}_{24}+\bar{\sigma}_{25})\right]\frac{\pi(\lambda)^2(\gamma_H/2)\sqrt{\pi}}{ku}, \tag{12}$$

where $\gamma_N=1/\tau$. The saturation intensity I_S for a given transition can be obtained from $I_S=I/S_{ij}$. All quantities appearing in the above expression are known and so there are no unknown parameters in this formulation. Absorption coefficients of successive slices were calculated by combining Eqs. (8) and (12). We have plotted % changes in the calculated values of the pump absorption coefficient at frequencies which correspond to the positions of the Lamb-dip transitions as a function of the position in the sodium cell at 120 and 169 °C in Fig. 3. The % change at a given frequency is calculated with respect to the unsaturated absorption coefficient at that frequency. There is scope of genuine confusion in the interpretation of Figs. 3(a) and 3(b) and in the discussion that follows. The narrow resonances can be seen only in the presence of counterpropagating pump and probe beams. Here we are discussing the changes in the absorption coefficient due to the presence of the pump beam alone. So, any reference to Lamb-dip transitions in this section actually refers to the frequencies at which the Lamb-dip resonances occur in a pump-probe experiment.

We find near degeneracy between the LD1 and LD2 plots and also between the LD3 and LD4 plots. This is because the pump absorption coefficients are calculated under Doppler-limited conditions. The pump beam is the only beam present for these calculations. For any setting of the laser frequency within the overall $D1$ profile, the pump gets absorbed by all transitions. The LD3 and LD4 frequencies being very close show nearly the same absorption despite the fact that the inherent cross section for the LD3 transition is one-fifth of the cross section of the LD4 transition. What actually happens is that when the laser is in resonance say with the zero velocity group of atoms at the frequency of the LD1 transition, it is also in resonance simultaneously at the frequency which corresponds to the transition LD2 for the groups of atoms which see the pump appropriately Doppler shifted. Since these two transitions are very close in frequency (189

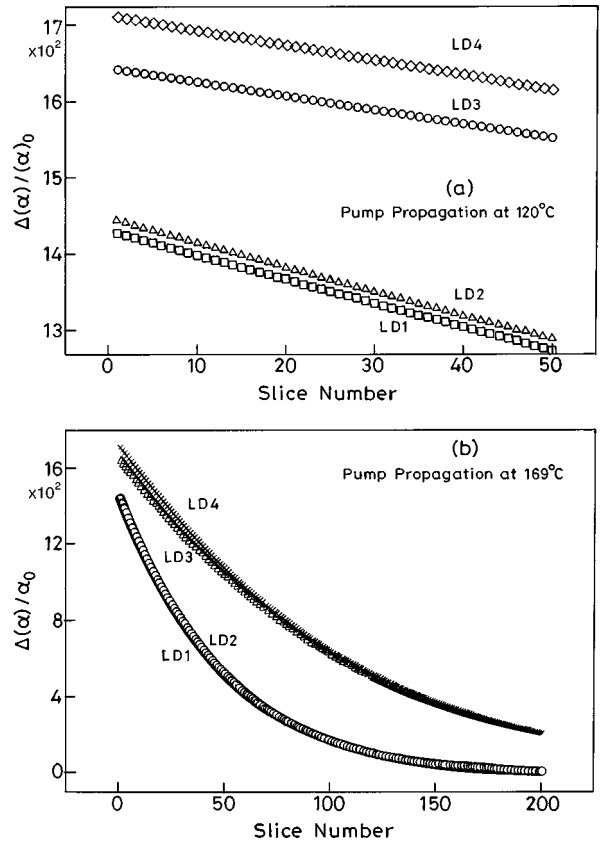

FIG. 3. Calculated changes in the absorption coefficient of the pump. The 10-cm-long cell is divided into 50 and 200 slices for calculations at 120 and 169 °C, respectively. The changes are calculated with respect to the unsaturated absorption coefficients. The labels LD1, LD2, LD3, and LD4 refer to the frequencies at which the Lamb-dip resonances occur in a pump-probe experiment.

MHz apart), the number of atoms contained in these two groups is nearly equal. The same argument holds for the LD3 and LD4 transition. At 120 °C we find rather small overall depletion (about 11% for the LD1 and LD2 transitions and 6% for the LD3 and LD4 transitions). All portions of the cell are nearly equally absorbing and we expect uniform optical pumping in the cell at this temperature. At 169 °C, the situation is quite different. The pump beam is rapidly depleted (98.9% absorption at the LD1 and LD2 transition frequencies and 88.7% absorption at the LD3 and LD4 transition frequencies) at this temperature. The degree of saturation and optical pumping is expected to be nonuniform. The % changes in the absorption coefficient at the LD1 and LD2 transition frequencies fall from 14% at the entrance of the cell to nearly 0% at the other end of the cell [Fig. 3(b)]. The corresponding numbers for the LD3 and LD4 transition frequencies are 17% and 3%, respectively. At this temperature the last quarter of the cell remains almost completely unsaturated and hardly develops any optical pumping. As a result, the counterpropagating probe beam is made substantially weak by the time it is able to interact with the pumped atoms. These calculations were carried out for the conditions of our experiment and by dividing the sodium cell into 50 slices for 120 °C and into 200 slices for 169 °C. This corresponds to a maximum linear absorbance of about 2% across each slice under the most unfavorable conditions.

B. Probe absorption coefficient

In the preceding subsection we have described in detail the procedure to calculate the pump absorption coefficient in each slice of the sodium cell. It is therefore possible to obtain the spatial variation of the extent of saturation and hence of optical pumping inside the cell. The optical pumping generated in the cell exists as long as the pump beam exists in the cell. We can monitor the spatial profile of the optical pumping by introducing a counterpropagating weak probe beam. The probe beam experiences absorption at a given position in the cell which is essentially determined by level populations as modified by the pump beam. Equation (11), however, cannot describe the probe absorption coefficient. As mentioned earlier, the simultaneous presence of the pump and the probe beams allows for the observation of crossover resonances in addition to the Lamb-dip resonances. We must add to Eq. (11) the remaining twelve integrals which give rise to the crossover resonances. There is another aspect which we must take into account for probe transmission. For the counterpropagating probe, the variable x appearing in Eq. (10) for the Lorentzians $\mathcal{L}_{ij}$ (but not $\mathcal{L}'_{ij}$, which are still determined by the pump) must be changed to ''$-x$,'' yielding

$$\mathcal{L}_{ij}(x)=\frac{(\gamma_H/2)^2}{(\Delta_{ij}+x)^2+(\gamma_H/2)^2} \tag{13}$$

for the probe beam propagation in the cell. This change has a profound effect on the contribution of various integrals in Eq. (9) towards the probe absorption coefficient. For example, the integrals involving double Lorentzians for any of the Lamb-dip resonances get significant contribution from x in the neighborhood of $x=0$ only. For $x\neq 0$, the two Lorentzians get displaced in opposite directions and so will have vanishingly small overlap. This amounts to saying that only the axially stationary atoms in the cell can simultaneously interact with the pump and the probe beams. Such atoms are selectively picked up in the VSOP experiment and lead to enhanced probe transmission when the laser is tuned to any of the Lamb-dip resonances. As soon as the laser is moved out of resonance, the probe beam essentially sees a thermal distribution of atomic populations.

When the laser is tuned to any one of the Lamb-dip resonances (say, the 2-4 resonance), then out of the four integrals appearing in Eq. (11) which involve double Lorentzians, only one which involves the product $\mathcal{L}_{24}\mathcal{L}'_{24}$ gives nonzero contribution. This is because the laser at a particular frequency can be in resonance with only one transition for the stationary atoms. However, the remaining four integrals in Eq. (11) which have only one Lorentzian do contribute to this resonance. After solving these integrals, the following expressions for the probe absorption coefficients of the LD1 and LD3 resonances were obtained:

$$\alpha_{2\to4}=\frac{(IN_2^0)\tau_e}{4h\nu}\frac{\sqrt{\pi}}{ku}\left(\frac{\gamma_H}{2}\right)^3\sigma_{24}\overline{\sigma}_{24}\left(2+\frac{T}{\tau}-T\Gamma_{42}\right)\left(1+\frac{1}{\sqrt{1+S_{24}}}\right)\left(\frac{e^{-(\Delta_{24}/ku)^2}}{4\Delta_{24}^2+(\gamma_H/2)^2[1+\sqrt{(1+S_{24})}]^2}\right)$$
$$+\int_{-\infty}^{\infty}N_1^0\overline{\sigma}_{14}\mathcal{L}_{14}(x)dx+\int_{-\infty}^{\infty}N_1^0\overline{\sigma}_{15}\mathcal{L}_{15}(x)dx+\int_{-\infty}^{\infty}N_2^0\overline{\sigma}_{24}\mathcal{L}_{24}(x)dx+\int_{-\infty}^{\infty}N_2^0\overline{\sigma}_{25}\mathcal{L}_{25}(x)dx, \quad (14)$$

$$\alpha_{1\to4}=\frac{(IN_1^0)\tau_e}{4h\nu}\frac{\sqrt{\pi}}{ku}\frac{4}{3}\left(\frac{\gamma_H}{2}\right)^3\sigma_{14}\overline{\sigma}_{14}\left(2+\frac{T}{\tau}-T\Gamma_{41}\right)\left(1+\frac{1}{\sqrt{1+S_{14}}}\right)\left(\frac{e^{-(\Delta_{14}/ku)^2}}{4\Delta_{14}^2+(\gamma_H/2)^2[1+\sqrt{(1+S_{14})}]^2}\right)$$
$$+\int_{-\infty}^{\infty}N_1^0\overline{\sigma}_{14}\mathcal{L}_{14}(x)dx+\int_{-\infty}^{\infty}N_1^0\overline{\sigma}_{15}\mathcal{L}_{15}(x)dx+\int_{-\infty}^{\infty}N_2^0\overline{\sigma}_{24}\mathcal{L}_{24}(x)dx+\int_{-\infty}^{\infty}N_2^0\overline{\sigma}_{25}\mathcal{L}_{25}(x)dx. \quad (15)$$

Similar expressions for the (1-5) and (2-5) Lamb-dip resonances can be obtained. For all Lamb-dip resonances, the probe absorption coefficient is found to decrease with respect to the off-resonance probe absorption. The absorption coefficients for the special nonzero velocity groups giving rise to the crossover resonances can also be obtained. But in this case, the probe beam transmission can increase or decrease with respect to off-resonance transmission depending on the nature of the crossover resonance.

The probe absorption coefficient for the nth slice in the cell can be calculated iteratively by a procedure similar to the one used for the pump beam,

$$I_n^{\text{probe}}(\text{in})=I_{n+1}^{\text{probe}}(\text{out})=I_{n+1}(\text{in})e^{-(\alpha_{n+1}\Delta z)}. \quad (16)$$

The difference in the slice order in this equation and in Eq. (8) for the pump beam reflects the fact that the probe counterpropagates the pump. The % changes in the absorption coefficient of the probe beam as a function of the position in the cell are calculated with respect to the absorption coefficients just outside the narrow resonances. These are shown in Fig. 4. The probe propagation effects are similar (but not exactly identical) to those found for the pump propagation. At 120 °C, there is an overall probe depletion of 12% for the LD1 and LD2 resonances and nearly 6.5% depletion for the LD3 and LD4 resonances. The corresponding figures for 169 °C are approximately 99% and 90%, respectively. These are slightly higher than the corresponding figures for the pump depletion. As for the pump, the probe absorption is nearly uniform in the cell at 120°. However, the change in probe absorption coefficient at 169 °C approaches zero value halfway in the cell for the LD1, LD2, and LD3 resonances. But the striking difference in probe absorption lies in the fact that the probe absorption coefficient and its % changes are different for all the Lamb-dip resonances. The kind of degeneracy noticed in the pump plots (Fig. 3) is absent here. This is attributed to the fact that unlike for the pump, the probe absorption is calculated under Doppler-free conditions because the pump and the probe beams interact with only special velocity groups of atoms for these resonances.

V. PROBE TRANSMISSION PROFILES

We have described in the preceding section how the probe absorption coefficient at any setting of the laser frequency can be calculated in the presence of a counterpropagating pump. The presence of narrow Lorentzians in expressions (14) and (15) for the absorption coefficient suggests the existence of sharp line features riding over broad absorption profiles. The FWHM of these sharp features is of the order of the natural linewidth γ_H with some power broadening. The absorption coefficients can be calculated over the entire range of frequencies of the $D1$ transition. The spectral profile of a narrow resonance can be generated be subtracting from the calculated probe intensities over the range of a narrow resonance the probe intensity in the immediate neighborhood of this resonance. Since these resonances are quite narrow, there is no difficulty in identifying the proper background transmission. However, in order to compare the calculated transmission profiles of the narrow resonances with

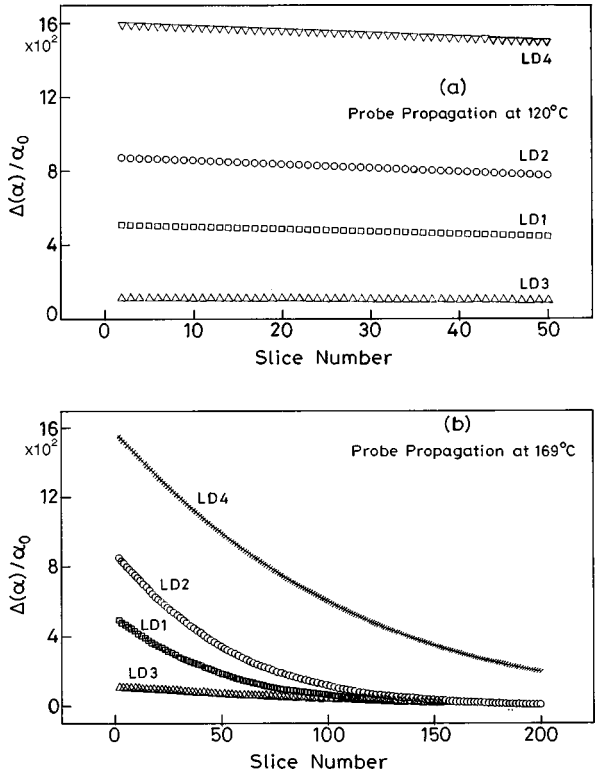

FIG. 4. Calculated profiles of changes in the probe absorption coefficient across the cell length of 10 cm. The cell is divided into 50 and 200 slices for calculation at 120 and 169 °C, respectively. The changes are calculated with respect to the unsaturated absorption coefficient.

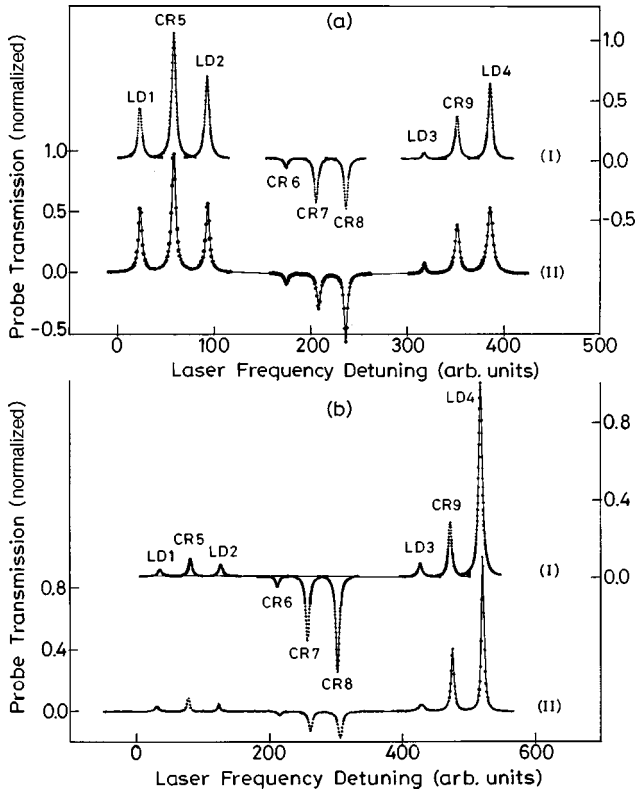

FIG. 5. Theoretical (I) and experimental (II) profiles of the $D1$ transition of sodium. (a) 120 °C (corresponding to $N=1\times10^{10}$ atoms/cm^3), (b) 169 °C ($N=3.4\times10^{11}$ atoms/cm^3). The vertical scales on the left are for the experimental profiles (II) and those on right are for the theoretical profiles (I).

those observed experimentally, it is necessary to express the vapor density (N_0) in terms of the cell temperature—the quantity actually at our disposal. For this purpose we have used the following relation:

$$\ln(N^0)=53.58-\frac{9.42\times10^3}{T'}-\ln T', \tag{17}$$

where N^0 is the number density or the population density as defined earlier and T' is the temperature in K. The consistency of Eq. (17) with standard vapor density-temperature curves was checked.

A. Low-temperature profiles

We have chosen 120 °C to represent the low-temperature limit. Recorded profiles at still lower temperatures had low signal-to-noise ratio. Figure 5(a) shows the recorded probe profiles (curve II) for all narrow resonances at 120 °C. For comparison, we have also included the calculated profiles (curve I). The two profiles are vertically displaced for better visual comparison. It is seen that there is excellent overall agreement between the calculated profiles and those observed at 120 °C. However, some discrepancies can be noticed. For example, the peak depth of the observed CR7 crossover resonance is nearly half as much as the observed peak depth of the CR8 crossover resonance, whereas the calculated depths for these resonances are nearly equal. A certain degree of power broadening can be noticed in the recorded profiles. The presence of some pedestal in the experimentally observed profiles over which the narrow resonances ride can be noticed. This feature is not apparent in the calculated profiles because each resonance was calculated independently and displayed next to the adjacent one. Table III shows a detailed comparison between the calculated and observed features of the profiles at this temperature. To facilitate comparison, we have taken the peak height of the strongest transition, namely the CR5 resonance, as having value 1 in the experimental and calculated profiles. We see generally good agreement between the values of the corresponding quantities appearing in these tables. We note in passing that at this temperature, the narrow resonances in the first group consisting of the LD1, LD2, and CR5 resonances are somewhat stronger than the corresponding resonances in the group consisting of the LD3, LD4, and CR9 resonances. In particular, the strongest line of the first group (CR5) is considerably stronger than LD4, which is the strongest resonance of the second group. We shall return to this observation later.

TABLE III. Observed and calculated amplitudes and areas of narrow resonances at 120 °C. Calculated amplitudes and areas are for $N_0=10^{10}$ atoms per cm^3, which corresponds to the cell temperature of 120 °C. For normalization, the observed and calculated amplitudes of the crossover resonance CR5 are taken as unity.

	Observed amplitude	Calculated amplitude	Observed area	Calculated area
LD1	0.53	0.40	3.7	2.7
LD2	0.57	0.67	4.1	5
LD3	0.08	0.05	0.44	0.31
LD4	0.55	0.64	5.8	4.9
CR5	1.0	1.0	7.8	7.6
CR6	0.09	0.08	0.64	0.47
CR7	0.29	0.37	2.1	2.4
CR8	0.56	0.42	3.5	2.8
CR9	0.40	0.36	3.4	2.7

B. High-temperature profiles

The recorded profiles of the narrow resonances at 169 °C and calculated profiles at $N_0=3.4\times10^{11}$ atoms/cm^3 are shown vertically displaced in Fig. 5(b). Once again we find good agreement between the two sets. However, the observed peak depths of the CR7 and CR8 crossover resonances are less than half the values predicted by the five-level model. At this point, we have no explanation for this discrepancy. A more detailed comparison of the peak depths and areas under the resonances can be seen in Table IV.

Here, we have normalized the peak heights to the peak height of the LD4 resonance, which is the strongest resonance at this temperature. As pointed out earlier, except for the central group of resonances (CR6, CR7, and CR8), the agreement between the observed and calculated peak heights and areas at 169 °C is nearly as good as for the lower temperature (120 °C) profiles.

C. Spectral changes with temperature

Two intriguing aspects of probe transmission can be noticed from Fig. 2. The probe transmission for any resonance

TABLE IV. Observed and calculated amplitudes and areas of narrow resonances at 169 °C. Calculated amplitudes and areas are for $N_0 = 3.4 \times 10^{11}$ atoms per cm^3, which corresponds to the cell temperature of 169 °C. For normalization, the observed and calculated amplitudes of the Lamb-dip resonance LD4 are taken as unity.

	Observed amplitude	Calculated amplitude	Observed area	Calculated area
LD1	0.03	0.03	0.34	0.28
LD2	0.05	0.06	0.26	0.53
LD3	0.04	0.07	0.64	0.56
LD4	1.0	1.0	6.5	9.6
CR5	0.08	0.09	0.52	0.82
CR6	0.03	0.05	0.26	0.45
CR7	0.12	0.32	1.29	3.0
CR8	0.16	0.5	1.94	4.8
CR9	0.4	0.28	3.1	2.5

first increases and then decreases as the cell temperature is increased from 110 to 169 °C. Further, the probe transmission for the CR9 and LD4 resonances is somewhat smaller than the transmission for the CR5 and LD2 resonances, respectively, at 120 °C, but at 169 °C the CR9 and LD4 resonances are considerably stronger than any other resonance in the spectrum. Thus there is some sort of reversal of the relative strengths of the resonances at the higher temperature. Figure 6 shows the calculated probe transmission for the narrow resonances for three atomic concentrations which roughly correspond to cell temperatures of 110, 147, and 169 °C, respectively. We see that the calculated probe transmission profiles do show at least qualitatively all the features observed experimentally (Fig. 2). To that extent our model correctly predicts the changes in the probe transmission as a function of the temperature and perhaps nothing more needs to be said about these aspects. However, we would like to understand exactly what happens to bring out these rather intriguing changes in the spectrum.

In order to appreciate better the nature of spectral changes with temperature, we consider sodium cells of different lengths and calculate the probe transmission at various temperatures. For a cell of length L divided into n slices of equal width, the recorded signal for probe transmission at a given frequency corresponds to

$$I_{\text{signal}} = I \ \ (\text{first slice}) - I_0 e^{-\alpha_0 L}, \tag{18}$$

where I (first slice) is the probe intensity as it emerges out of the cell and I_0 is the probe intensity entering the cell. The second term in Eq. (18) represents the probe transmission in the absence of the pump. Since our experiment records only changes in probe transmission with respect to the unpumped condition, this term has to be subtracted. The calculated peak probe transmissions for LD2 and LD4 resonances as a function of the cell length are shown in Fig. 7 at 120 and 169 °C. To calculate the peak probe transmission at a given temperature, the number density was kept constant as the cell length was increased. Table V gives the ratio of the peak heights of the LD2 and LD4 resonances at 120 and 169 °C for different cell lengths. In the absence of beam attenuation, this ratio is expected to be close to the ratio of the degeneracies of levels

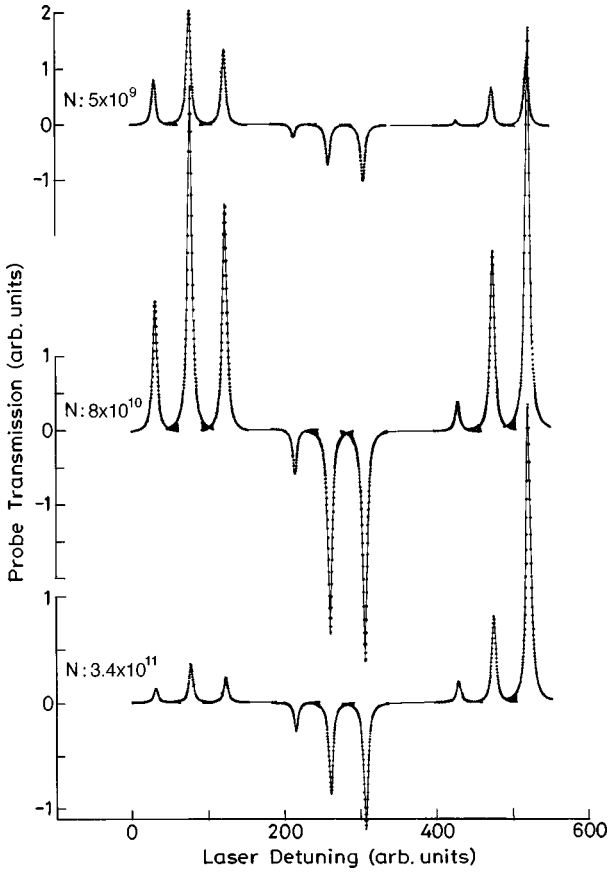

FIG. 6. Calculated profiles of the $D1$ transition of sodium for $N = 5 \times 10^9$ atoms/cm^3, $N = 8 \times 10^{10}$ atoms/cm^3, $N = 3.4 \times 10^{11}$ atoms/cm^3, corresponding to temperatures near 110, 147, and 169 °C, respectively. These plots should be compared with the corresponding temperature plots in Fig. 2. All plots in this figure are drawn to the same scale.

2 and 1 in the five-level model (see Fig. 1). It is desirable at this stage to state what we expect to learn from these calculations. We have already seen that at 120 °C the cell is nearly uniformly pumped because the pump beam absorption is rather low (about 12%). In the absence of significant attenuation along the length of the cell, the relative transmission of the probe beam for different resonances should not change with the length of the cell. In particular, we should expect the ratio of the LD2 to LD4 transmissions to remain unchanged when the cell length is increased. However, at higher temperatures the cell length should play a crucial role because of severe attenuation of the pump beam as it propagates in the cell. If the pump attenuation is significantly different for different transitions, we can expect the reversal effects to begin at different lengths for different transitions for a particular value of the cell temperature. From Fig. 7 we see that at 120 °C, the strength of any transition increases monotonically as the cell length is increased. The monotonic nature at this temperature arises because with increasing length more and more atoms become available for pumping and the pump beam remains strong enough throughout the cell length to create pumping in the absence of any significant attenuation. The ratio of the LD2 to LD4 strengths is close to the expected value of 1.33 and remains essentially unchanged as the cell length is increased from 0.2 to 10 cm. The slight

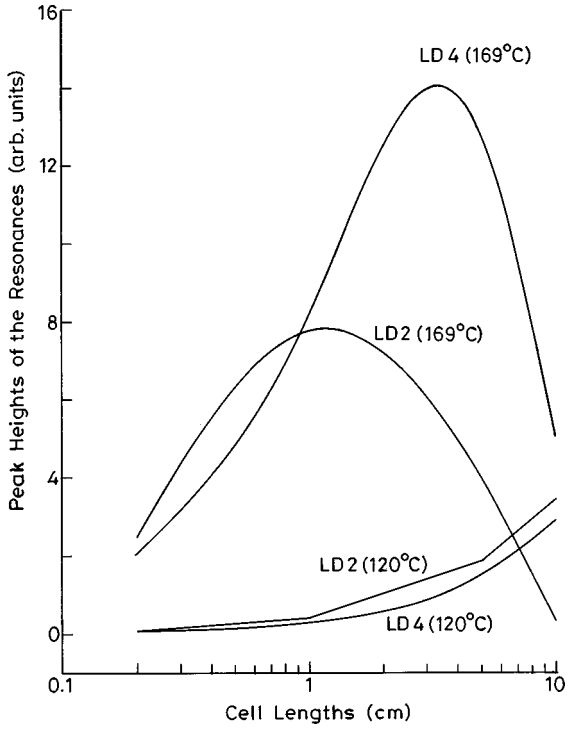

FIG. 7. Calculated peak heights of the Lamb-dip resonances LD2 and LD4 at 120 and 169 °C for cells of varying lengths.

change (about 7%) in this ratio with length is due to the presence of a small amount of attenuation even at this temperature. Similar calculations at higher temperatures reveal that as the cell length is increased, the strength of any resonance first increases and then begins to decrease. But this changeover takes place at different lengths for different transitions. The LD2 resonance shows this effect at a much smaller length as compared to the LD4 resonance. Because of severe attenuation at these temperatures, the pump is not able to efficiently pump the atoms, leading to a decrease in the strength of the signal. At 169 °C the ratio of the LD2 to LD4 strengths decreases from a value of 1.21 to 0.07 as the cell length is increased from 2 mm to 10 cm. Thus at this temperature, the reversal takes place just before the cell length approaches 1 cm. Figure 7 shows that whereas the LD2 resonance begins to decrease in strength as the cell length exceeds 1 cm, the LD4 resonance continues to gain strength until the cell length approaches 3 cm and then its strength decreases rather abruptly. As a result the LD2 resonance becomes quite weak by the time the probe beam exits the cell of 10 cm. This is exactly what we find experimentally. Let us now try to understand why the reversal in the ratio of LD2 to LD4 strengths takes place in the presence of significant beam attenuation. The LD1 and LD2 transitions originate from level 2 and LD3 and LD4 transitions originate from level 1 in the five-level scheme. Level 1 has a degeneracy of 3 and level 2 has an effective degeneracy of 4 for excitation with circularly polarized light. Thus a larger number of atoms (in the ratio of 4:3) are available for interaction when the laser is tuned to the LD1 and LD2 resonances as compared to the case when the laser is tuned to the LD3 and LD4 resonances. At lower temperatures the available number of atoms decides the relative strengths of the signals and hence the ratio of the peak heights of the LD2 to LD4 resonances is close to the expected value of 1.33 while at higher temperatures it is the beam attenuation which decides the strength of the signal. This is so because the higher number of atoms available at higher temperatures drastically attenuates the beam. This happens selectively for the LD1,LD2 and LD3,LD4 resonances. The beam is attenuated much more when the laser is tuned to the former pair of resonances because of the more numerous atoms available for the absorption at these transitions. This leads to a highly nonuniform spatial profile of optical pumping in the cell at 169 °C as revealed by Figs. 3 and 4. Thus although the basic cause of reversal of the relative strengths of these pairs of resonances is the higher degeneracy of level 2, its effect is manifested only in the presence of significant beam depletion in the cell. We have selected LD2 and LD4 resonances for the present discussion because the cross sections for these transitions are nearly equal and the changes in the probe transmission for these resonances can be at least qualitatively understood in terms of the degeneracies of the levels. However, our quantitative results apply to all narrow resonances. Referring to Fig. 2, we remark that the initial increase of the signals for all resonances is due to the increasing number of atoms available for absorption with increasing temperature. At still higher temperature, beam depletion becomes so strong that that it is hardly able to saturate the atoms. This results in the decrease of the signal. It is therefore possible to understand in physical terms the changes in the probe transmittance as a function of temperature for all narrow resonances.

TABLE V. Ratio of peak heights of the LD2 and LD4 resonances for different cell lengths at 120 and 169 °C. LD2 to LD4 peak height ratio.

drag \ Cell length (mm)	0.2	10	50	100	Temperature (°C)
	1.29	1.27	1.23	1.19	120
	1.21	0.96	0.31	0.07	169

D. Sum rules

In Ref. [1], some relationships (23)–(27) between the integrated absorption coefficients of the crossover resonances and the Lamb-dip resonances were derived. Since these relations provide some internal checks for the predictions of the five-level model, we might treat them as some kind of sum rules. These relationships were obtained in the limit of weak beam absorption ($\alpha_0 L \ll 1$), where α_0 is the unsaturated or low power absorption coefficient and L is the cell length. This condition holds at lower temperatures near 120 °C. Now that we have discussed the beam depletion effects in great detail, perhaps a second look at these relations is warranted. In the earlier work all Gaussian factors $G(x)$ appearing in the expression for the absorption coefficient were replaced by unity. This is a reasonable approximation for all Lamb dips and for the crossover resonances CR5 and CR9, but this certainly does not hold for the central crossover resonances CR6, CR7, and CR8. It is only these later resonances for which the discrepancies were found. The modified sum rules obtained by using the appropriate values of the Gaussian factors and their verification are shown in

TABLE VI. Verification of the predictions of the five-level model (at 120 °C).

Measured areas of the crossover resonances (in arb. units)	Areas of the crossover resonances as obtained from Lamb-dip areas (arb. units)
$\mathcal{A}_5$	$\mathcal{A}_1+\mathcal{A}_2$
9.7×10^{-5}	9.7×10^{-5}
$\mathcal{A}_6$	$(-\frac{2}{15}\mathcal{A}_1-3\mathcal{A}_3)\times0.38$
-5.0×10^{-6}	-7.6×10^{-6}
$\mathcal{A}_7$	$(-\frac{2}{3}\mathcal{A}_1-\frac{9}{16}\mathcal{A}_4)\times0.3-(\frac{16}{75}\mathcal{A}_2-3\mathcal{A}_3)\times0.46$
-2.2×10^{-5}	-3.0×10^{-5}
$\mathcal{A}_8$	$(-\frac{16}{15}\mathcal{A}_2-\frac{9}{16}\mathcal{A}_4)\times0.38$
-3.8×10^{-5}	-3.4×10^{-5}
$\mathcal{A}_9$	$5\mathcal{A}_3+\frac{1}{5}\mathcal{A}_4$
3.8×10^{-5}	4.0×10^{-5}

Table VI. It is seen that the discrepancies for the central crossover resonances are resolved to a great extent. Some discrepancy remains for the crossover resonance CR6 but this resonance is much weaker than the remaining crossover resonances. We have no explanation for this discrepancy at the present time. However, we feel that the assumption that the probe beam does not affect level population may no longer hold. How an inclusion of this effect will affect only the central crossover resonances is certainly not clear, but such a study is worth attempting in the future.

VI. SUMMARY

The Doppler-free spectrum of the $D1$ transition was studied as a function of temperature covering the range from 110 to 169 °C. A nonmonotonic behavior of the strengths of the narrow resonances as a function of temperature was found. At 120 °C, the group of transitions comprising the LD1, CR5, and LD2 resonances is somewhat stronger than the group comprising LD3, CR9, and LD4 resonances. However, a complete reversal of their strengths takes place at 169 °C. In view of the high level of beam depletion (as much as 99% for some of the resonances) in the cell, the beam propagation effects were considered by dividing the sodium cell into 200 subcells at 169 °C. This Beer-Lambert law was applied to each subcell in succession. This procedure fully accounts for the beam depletion effects. Numerical solutions were obtained for pump-and-probe transmission. It was possible to achieve excellent agreement between the calculated and experimentally recorded line profiles of all narrow resonances in the complete range of temperature used in our investigations. It was found that because of higher degeneracy of the upper ground level in the five-level model, the pump beam experiences considerably higher attenuation for transitions starting from this level as compared to the transitions starting from the lowest ground level. This fact is responsible for the peculiar changes in the probe transmission as a function of temperature. Further it has been possible for us to provide better experimental verification of the modified sum rules representing relationships among the frequency integrated absorption coefficients of crossover and the Lamb-dip resonances.

APPENDIX

$$S_{14}=\frac{\sigma_{14}IT\tau_e}{12h\nu}\left(-4\Gamma_{41}+\frac{4}{\tau_e}+\frac{4}{T}\right), \tag{A1}$$

$$S_{15}=\frac{\sigma_{15}IT\tau_e}{12h\nu}\left(-4\Gamma_{51}+\frac{4}{\tau_e}+\frac{3}{T}\right), \tag{A2}$$

$$S_{24}=\frac{\sigma_{24}IT\tau_e}{12h\nu}\left(-3\Gamma_{42}+\frac{3}{\tau_e}+\frac{4}{T}\right), \tag{A3}$$

$$S_{25}=\frac{\sigma_{25}IT\tau_e}{12h\nu}\left(-3\Gamma_{52}+\frac{3}{\tau_e}+\frac{3}{T}\right), \tag{A4}$$

$$S_{14}^1=\frac{T\tau_e}{12}\left[\frac{\sigma_{14}I}{h\nu}\left(\frac{4N_1^0}{T}\right)-\frac{12N_1^0}{T\tau_e}S_{14}\right], \tag{A5}$$

$$S_{15}^1=\frac{T\tau_e}{12}\left[\frac{\sigma_{15}I}{h\nu}\left(\frac{3N_1^0}{T}\right)-\frac{12N_1^0}{T\tau_e}S_{15}\right], \tag{A6}$$

$$S_{24}^1=\frac{T\tau_e}{12}\left[\frac{\sigma_{24}I}{h\nu}\left(\frac{4N_1^0}{T}+3\Gamma_{41}N_2^0-3\Gamma_{42}N_1^0+\frac{3N_1^0}{\tau_e}\right)-\frac{12N_1^0}{T\tau_e}S_{24}\right], \tag{A7}$$

$$S_{25}^1=\frac{T\tau_e}{12}\left[\frac{\sigma_{25}I}{h\nu}\left(\frac{3N_1^0}{T}+3\Gamma_{51}N_2^0-3\Gamma_{52}N_1^0+\frac{3N_1^0}{\tau_e}\right)-\frac{12N_1^0}{T\tau_e}S_{25}\right], \tag{A8}$$

$$S_{14}^2=\frac{T\tau_e}{12}\left[\frac{\sigma_{14}I}{h\nu}\left(\frac{4N_2^0}{T}+4\Gamma_{42}N_1^0-4\Gamma_{41}N_2^0+\frac{4N_2^0}{\tau_e}\right)-\frac{12N_2^0}{T\tau_e}S_{14}\right], \tag{A9}$$

$$S_{15}^{2}=\frac{T\tau_e}{12}\left[\frac{\sigma_{15}I}{h\nu}\left(\frac{3N_2^0}{T}+4\Gamma_{52}N_1^0-4\Gamma_{51}N_2^0+\frac{4N_2^0}{\tau_e}\right)-\frac{12N_2^0}{T\tau_e}S_{15}\right], \tag{A10}$$

$$S_{24}^{2}=\frac{T\tau_e}{12}\left[\frac{\sigma_{24}I}{h\nu}\left(\frac{4N_2^0}{T}\right)-\frac{12N_2^0}{T\tau_e}S_{24}\right], \tag{A11}$$

$$S_{25}^{2}=\frac{T\tau_e}{12}\left[\frac{\sigma_{25}I}{h\nu}\left(\frac{3N_2^0}{T}\right)-\frac{12N_2^0}{T\tau_e}S_{25}\right], \tag{A12}$$

$$S_{14}^{4}=\frac{T\tau_e}{12}4\frac{\sigma_{14}I}{h\nu}\left(\frac{N_1^0}{T}\right), \tag{A13}$$

$$S_{24}^{4}=\frac{T\tau_e}{12}3\frac{\sigma_{24}I}{h\nu}\left(\frac{N_2^0}{T}\right), \tag{A14}$$

$$S_{15}^{5}=\frac{T\tau_e}{12}\frac{\sigma_{15}I}{h\nu}\left(4\frac{N_1^0}{T}\right), \tag{A15}$$

$$S_{25}^{5}=\frac{T\tau_e}{12}\frac{\sigma_{25}I}{h\nu}\left(3\frac{N_2^0}{T}\right), \tag{A16}$$

$$\frac{1}{\tau_e}=\frac{1}{T}+\frac{1}{\tau}. \tag{A17}$$

[1] R. S. Gurjar and K. K. Sharma, Phys. Rev. A **53**, 969 (1996).

[2] S. Svanberg, G.-Y. Yan, T. P. Duffey, W.-M. Du, T. W. Hänsch, and A. L. Schawlow, J. Opt. Soc. Am. B **4**, 462 (1987).

[3] C. Schmidt-Inglesias, L. Roso, and R. Corbalan, Opt. Lett. **15**, 63 (1990).

[4] O. Di Lorenzo–Filho, P. C. de Oliveira, and J. R. Rios Leite, Opt. Lett. **16**, 1768 (1991).

[5] C. Schmidt-Iglesias, L. Roso, and R. Corbalan, Opt. Commun. **90**, 251 (1992).

[6] M. D. Lukin, M. Fleischhauer, A. S. Zibrov, H. G. Robinson, V. L. Velichansky, L. Hollberg, and M. O. Scully, Phys. Rev. Lett. **79**, 2959 (1997).

[7] W. W. Quivers, Jr., Phys. Rev. A **34**, 3822 (1986).

[8] L. Caiyan, S. Kröll, L. Sturesson, and S. Svanberg, Phys. Rev. A **53**, 1668 (1995).